Monthly Notices
of the
ROYAL ASTRONOMICAL SOCIETY

MNRAS **484,** 618–630 (2019)
Advance Access publication 2019 January 16

doi:10.1093/mnras/sty3474

Differential rotation of Kepler-71 via transit photometry mapping of faculae and starspots

S. M. Zaleski [1]★ A. Valio,[2] S. C. Marsden[1] and B. D. Carter[1]

[1] *University of Southern Queensland, Centre for Astrophysics, Toowoomba 4350, Australia*
[2] *Center for Radio Astronomy and Astrophysics, Mackenzie Presbyterian University, Rua da Consolação, 896 São Paulo, Brazil*

Accepted 2018 December 19. Received 2018 December 18; in original form 2017 November 16

ABSTRACT

Knowledge of dynamo evolution in solar-type stars is limited by the difficulty of using active region monitoring to measure stellar differential rotation, a key probe of stellar dynamo physics. This paper addresses the problem by presenting the first ever measurement of stellar differential rotation for a main-sequence solar-type star using starspots and faculae to provide complementary information. Our analysis uses modelling of light curves of multiple exoplanet transits for the young solar-type star Kepler-71, utilizing archival data from the *Kepler* mission. We estimate the physical characteristics of starspots and faculae on Kepler-71 from the characteristic amplitude variations they produce in the transit light curves and measure differential rotation from derived longitudes. Despite the higher contrast of faculae than those in the Sun, the bright features on Kepler-71 have similar properties such as increasing contrast towards the limb and larger sizes than sunspots. Adopting a solar-type differential rotation profile (faster rotation at the equator than the poles), the results from both starspot and facula analysis indicate a rotational shear less than about 0.005 rad d^{-1}, or a relative differential rotation less than 2 per cent, and hence almost rigid rotation. This rotational shear contrasts with the strong rotational shear of zero-age main-sequence stars and the modest but significant shear of the modern-day Sun. Various explanations for the likely rigid rotation are considered.

Key words: stars: activity – stars: rotation – stars: solar-type – starspots.

1 INTRODUCTION

Starspots and faculae are observable proxies of stellar magnetic activity in solar-type stars, providing a window to the internal dynamo. Starspots and faculae may be observed on cool stars with a convective envelope surrounding a radiative core (Berdyugina 2004; Balona & Obedigamba 2016). They are tracers of an unseen dynamo and markers of magnetic topology. Starspots and faculae are the surface emanations of internal magnetic fields caught in turbulent flows. They are areas of amplified magnetic fields which erupt through the stellar surface. Starspots and faculae differ thermally from the surrounding photosphere (Ortiz et al. 2002), with starspots appearing dark against a hotter and brighter photosphere and faculae appearing brighter than the photosphere.

Spots on the Sun have been observed for four centuries. Sunspot coverage and the latitudinal drift of the sunspot distribution have been correlated with long-term solar magnetic cycles (Maunder 1904; Hathaway 2015; Covas 2017). Magnetic activity in a solar-type interface dynamo is thought to be generated deep in the convective zone at the tachocline where rotation interacts with convective flows (Spruit 1997; Spuit 2011). Though the magnetohydrodynamic processes at work in the stellar interior are not fully understood, the convectively driven interface dynamos in late-type stars, slow rotators such as the Sun, are based on rotating, weakly magnetized differential flows (Uzdensky et al. 2010). Any large-scale dynamo model such the solar $\alpha\Omega$ dynamo, in which weak magnetic fields are amplified by shearing of field lines via differential rotation (Hubbard, Rheinhardt & Brandenburg 2011), twisted by the Coriolis effect and promoted to the surface via magnetic buoyancy, must allow the same magnetic features, dark spots, and bright faculae, to appear on the surface of stars with a convective envelope (Hubbard et al. 2011; Isik, Schmidtt & Schussler 2011; Shapiro et al. 2016). Thus, any $\alpha\Omega$ dynamo model that explains the magnetic activity of the Sun should be applicable to any rotating, convective solar-type star. Observations of solar-type stars expand the understanding of stellar processes, i.e. convection, rotation, and magnetism, and allow for the evaluation of commonality among dynamic properties of the Sun and other stars, thereby establishing a solar-stellar connection. An interface dynamo model may be constructed to agree with available solar data, but it will be limited by that same data. Solar data collected in this century reflect the Sun's current activity. The characteristics of starspots and faculae on magnetically active solar-

★ E-mail: shelley.zaleski@usq.edu.au

type stars will add to our understanding of the evolution of the Sun's magnetic activity.

The presence of starspots and faculae contribute to the overall stellar irradiance and light curve variance (Mehrabi, He & Khosroshahi 2017). The temporal change in starspot/facula coverage on the stellar surface is witnessed as periodic, sinusoidal trends in stellar light curves, with the degree of light curve modulation being indicative of magnetic activity level (Mehrabi et al. 2017). Studies of modulation in light curves recorded by the *Kepler* mission (Borucki 2010) have produced a wealth of information on stellar rotation rates and activity trends (McQuillan, Mazeh & Aigrain 2013, 2014; Reinhold, Reiners & Basri 2013; He, Wang & Yun 2015; Mehrabi, He & Khosroshahi 2017). During its approximately four years of data collection, from 2009 March to 2013 May, NASA's *Kepler* telescope gathered data for over 150 000 stars in a wide-field of view in the Cygnus–Lyra region. Though the primary goal of the *Kepler* mission was to discover terrestrial size planets in the habitable zones of Sun-like stars via the transit method (Borucki 2010), the abundance of data collected has supported the analysis of stellar behaviour over a range of spectral types and ages. *Kepler* collected data in two cadence modes, a long cadence (LC) of 29.4 min and a short cadence (SC) of 58.85 s. LC data are well suited to the analysis of large-scale trends, such as the periodicity and amplitude of light curve modulation due to magnetic activity. For *Kepler* G-type main-sequence stars with rotation periods of 10–20 d, for example, the periodicity and amplitude of light curve variation show a positive correlation for approximately 80 per cent of sampled stars (Mehrabi et al. 2017). The percentage of positive correlation stars is greatest for shorter stellar rotation periods and least for rotation periods longer than 20 d, inferring that magnetic activity decreases with age due to spin-down and decreasing $T_{\rm eff}$, though starspot stability increases as rotation slows. The active regions on G-stars are also larger and more stable than those on A and F stars (McQuillan, Aigrain & Roberts 2012; Giles, Collier Cameron & Haywood 2017). Analysis of starspot lifetime for FGKM stars with rotation periods approximately 10 and 20 d shows that starspots decay more slowly on cooler stars, commensurate with the diffusive mechanisms of the dynamo. For G-type stars, the majority of spots lasted up to 100 d, with few lasting as long as 300 d (Mehrabi et al. 2017).

While magnetic activity is evident in LC data, the fine detail indicative of faculae, single starspots, or groups of starspots is not discernible. Due to a high-sampling rate, SC data have the resolution to detect the presence of starspots and faculae in transit light curves. When an exoplanet occults starspots and/or faculae during its transit across the face of its host star, small variations appear in the in-transit portion of a stellar light curve. Starspots and faculae are seen as bumps and dips, respectively, in the transit light curve. An example of amplitude variation due to occulted magnetic structures is shown in Fig. 2. Starspot and facula physical characteristics of radius, intensity, and position may be modelled using the width, height, and time of variations (Silva 2003). Through the application of transit photometry mapping, these characteristics are translated into magnetic activity maps of the stellar surface. This methodology (see Section 3) has been used to assess surface activity and stellar rotation at transit latitudes for Kepler-17 (Valio et al. 2017), CoRoT-2 (Silva-Valio et al. 2010; Silva-Valio & Lanza 2011), and Kepler-63 (Estrela & Valio 2016).

Starspot and facula longitudes derived from SC data lie along the projected transit latitude, which is typically non-equatorial. Stellar rotation rates at transit latitudes may be calculated from starspot/facula longitudes in transit light curves commensurate with multiple, consecutive stellar rotations. Stellar differential rotation may be estimated when latitudinal rotation periods differ from that at the stellar equator. Simulations of differential rotation in spectral type G and K stars at 0.7 and 0.9 $M_{\odot}$, respectively, rotating at the solar rate show solar-like differential rotation, with the equator rotating more rapidly than the poles, e.g. Matt et al. (2011). Küker & Rüdiger (2005) modelled FGK stars for different solar masses and found that differential rotation is dependent on stellar temperature, i.e. convection zone depth, and only weakly dependent on rotation rate. The greater the stellar effective temperature and mass, the higher the shear and differential rotation (Barnes et al. 2005; Balona & Obedigamba 2016). The differential rotation of *Kepler* stars calculated by Reinhold et al. (2013) predominantly lies between 0.03 and 0.11 rad d^{-1} over the temperature range 3500–6000 K. They find wide scatter in differential rotation values from 0.4 to 3.0 rad d^{-1} at temperatures from 6000 to 7000 K. This is in agreement with Barnes et al. (2005), who predicted an exponential growth in differential rotation as a function of stellar temperature for young stars, and the observations of Marsden et al. (2011) and Waite et al. (2011). Barnes et al. (2005) also proposed that a decrease in differential rotation in later spectral types is due to a greater α-effect than Ω-effect.

To date, measurement of stellar rotation period and differential rotation has utilized spectroscopic and spectropolarimetric methods to build structural and magnetic maps of spotted stellar surfaces, Fourier domain methods applied to Doppler broadened line profiles, and photometric methods to analyse the periodic trends in light curves caused by starspots. Doppler Imaging (DI) and Zeeman Doppler Imaging (ZDI) have been used to map the surfaces of active cool stars. Their use, especially DI, tends to be limited to comparatively rapid rotators, as spatial resolution of the stellar surface decreases with slowing rotation. Nevertheless, DI and ZDI mapping can measure the differential rotation of moderately to rapidly rotating stars, e.g. Carter, Marsden & Waite (2015) and Hackman et al. (2016). Fourier transformed absorption profiles show distinct behaviour in the Fourier domain (Reiners & Schmitt 2002). This technique, however, is also limited to rotators with values of $v\sin i \geq 10$ km s^{-1}.

Photometric techniques used to study the effect of starspots on stellar light curves include phase tracking (Davenport, Hebb & Hawley 2015) and sine-fitting periods from Lomb–Scargle periodograms (Reinhold et al. 2013). These methods are applicable to a wide range of stellar rotation rates and magnitudes. Aigrain et al. (2015) employed various photometric methods, including Lomb–Scargle periods, auto-correlation functions, and wavelet power spectra, in a blind study to extract rotation rates and differential rotation from simulated *Kepler* light curves. The study showed limited agreement among methods in the computation of differential rotation.

Our methodology is based on individual magnetic features as they appear in transit light curves rather than on broader photometric trends. We have detected and mapped both facula and starspot signatures in the transit light curves for Kepler-71 and thus present the estimation of transit latitude rotation periods and differential rotation from the longitudinal movement of individual facula as well as starspots. We discuss the differential rotation of Kepler-71 relative to theoretical predictions and published observational values (see Section 5).

2 KEPLER-71 OBSERVATIONAL DATA

Kepler-71 is a *Kepler*-band magnitude 15, solar-type G star with a single hot Jupiter in a 3.91 d orbit. The parameters of the host star-exoplanet system are given in Table 1. Kepler-71 has approximately

Table 1. Star-exoplanet parameters of the Kepler-71 system.

Parameter	Value	Ref.
Star		
Spectral type	G7V–G9V	1
Mass ($M_\odot$)	$0.997^{+0.03}_{-0.07}$	2
Radius ($R_\odot$)	0.887 ± 0.05	2
Effective temp (K)	5540 ± 120	2
Rotation period (d)	19.773 ± 0.008	3
Age (Gyr)	2.5–4.0	4, 5
Limb darkening coeff, u_1	0.431 ± 0.008	3
Limb darkening coeff, u_2	0.287 ± 0.005	3
Planet		
Mass ($M_{\rm Jup}$)	n/a	
Radius ($R_{\rm Jup}$)	1.1987 ± 0.0044	3
Radius ($R_{\rm star}$)	0.1358 ± 0.0005	3
Semimajor axis (au)	$0.05029^{+0.00002}_{-0.00006}$	3
Semimajor axis ($R_{\rm star}$)	$12.186^{+0.006}_{-0.015}$	3
Inclination angle (°)	$89.557^{+0.005}_{-0.003}$	3
Orbital period (d)	$3.905079476^{+8e-6}_{-9e-6}$	6

1: Howell et al. (2010), 2: Mathur et al. (2016), 3: Fit by authors in this work, 4: Meibom et al. (2015), 5: Guinan & Engle (2009), and 6: Müller et al. (2013).

the same size and mass as the Sun with 0.887 $R_\odot$ and 0.997 $M_\odot$, respectively, with an orbiting planet of radius $1.14R_{\rm Jup}$. Howell et al. (2010) first noted rotational modulation in the raw *Kepler* light curves for Quarter 6 and intensity fluctuations indicative of starspots in the transit well of phase folded light curves. Both McQuillan et al. (2013) and Holczer et al. (2015) calculated a stellar rotation period of 19.77 d via the autocorrelation of light curve modulation. Holczer et al. (2015) noted another prominent peak in the power spectrum at 9.9 d, possibly due to active regions that are 180° out-of-phase (discussed in Section 4.4).

The age of Kepler-71 is estimated to be between 2.5 and 4.0 Gyr. The lower bound of 2.5 Gyr was determined by Meibom et al. (2015) in their study of stellar rotation in the 2.5 billion year old open cluster NGC 6819. The average rotation period of 18.2 d for the observed solar mass stars in that cluster served to establish a rotation rate benchmark for the Sun at 2.5 Gyr. The upper bound of 4.0 Gyr is taken from the study of main-sequence G-star rotation rate versus age presented by the *Sun in Time* program (Guinan & Engle 2009).

We extend the work of Howell et al. (2010) and Holczer et al. (2015) by quantifying starspot activity on Kepler-71. The NASA Exoplanet Archive contains pre-conditioned light curve data for Kepler-71 spanning *Kepler* Quarters 1–17. The *Kepler* pre-conditioning pipeline removes systematic artefacts of the instrumentation onboard the *Kepler* spacecraft from raw aperture data to yield Pre-search Data Conditioning Simple Aperture Photometry (PDCSAP) flux values that preserve stellar variations and astrophysics (Jenkins et al. 2010; Smith et al. 2012; Stumpe et al. 2012). The PDCSAP SC data provide both uninterrupted coverage for time periods during which multiple transits are observed and the temporal resolution required for the detection of occultations lasting on the order of minutes. Of interest to this investigation are the detrended PDCSAP SC light curves in *Kepler* Data Release 25 (Thompson 2016) available for Quarter 6 (2010 June 24–2010 September 22), Quarter 7 (2010 September 23–2010 December 22), Quarter 13 (2012 March 29–2012 June 27), Quarter 14 (2012 June 28–2012 October 3), Quarter 15 (2012 October 5–2013 January 11), Quarter 16 (2013 January 12– 2013 April 8), and Quarter 17 (2013 April 9–2013 May 11). The SC light curves for those quarters, as shown in Fig. 1, comprise observations for approximately 500 d and contain 117 complete, uninterrupted transits out of 261 total transits from the beginning of Quarter 6 to the end of Quarter 17.

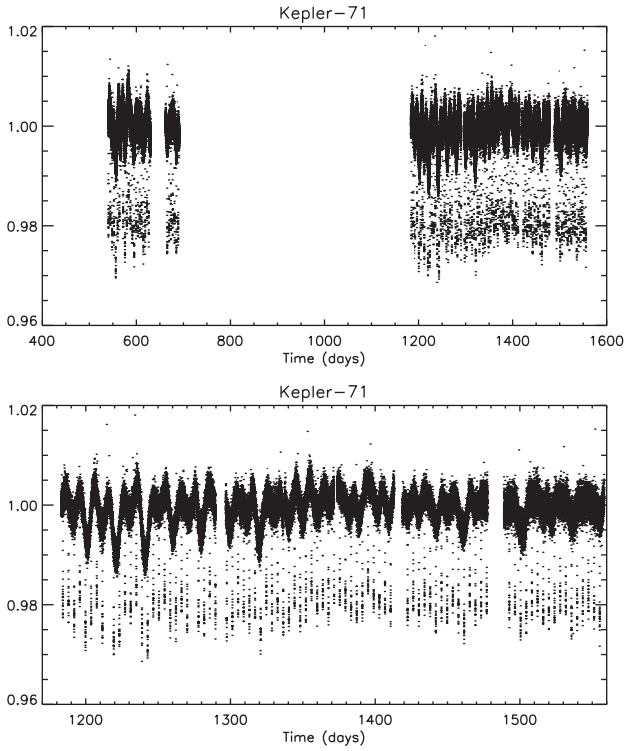

Figure 1. *Top:* SC light curves for Kepler-71 for Quarters 6–7 and Quarters 13–17. *Bottom:* Enlargement of the SC light curves for Quarters 13–17.

Late-type stars, such as Kepler-71, display a stochastic stellar variability commensurate with surface activity (McQuillan et al. 2012). As such, we require that the transit well be deep enough to detect relatively small modulations due to faculae and starspots. Deep transits are evident in Fig. 1. The mean normalized flux decrease for Kepler-71 is approximately 2 per cent from ingress to the bottom of the transit well. The example given in Fig. 2 for Transit 3 shows an approximate 2.5 per cent overall decrease in normalized flux. Mid-transit time ($t = 0$) corresponds to transit epoch 547.3541 BKJD [Barycentric Kepler Julian Date defined as Barycentric Julian Day (BJD) minus an offset of 2454833 corresponding to 12:00 On 2009 January 1 UTC]. The flux changes due to the starspot at midtransit and the faculae at times -1.0 h and $+0.8$ h from transit centre, respectively, are on the order of 0.4, 0.3, and 0.2 per cent. The modelled red curve is described in the next section.

3 THE MODEL

The light curve model developed by Silva (2003) is used to determine the physical characteristics of in-transit photometric variations caused by the passage of an exoplanet across a stellar disc. The model's flexibility allows for the generation of transit light curves for an exoplanet traversing unspotted, spot-dominated, and facula-dominated stellar surfaces. Thus, the model may be used for solar-type stars of varying magnetic activity. As solar-type stars evolve along the main-sequence, losing angular momentum, magnetic activity moves from spot dominance to facula dominance

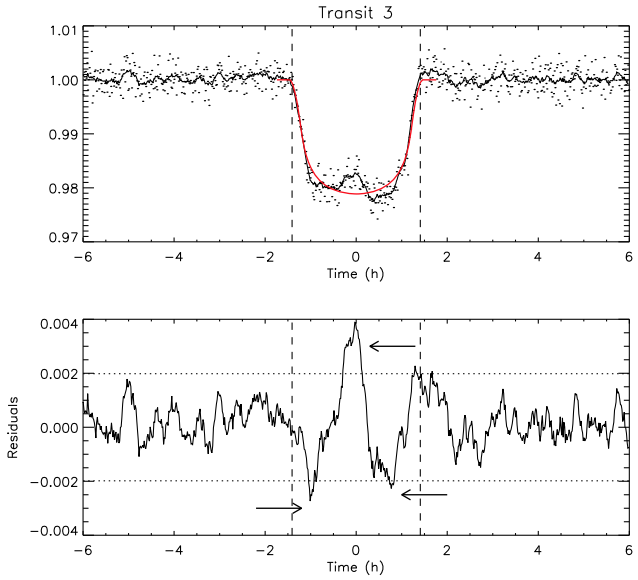

Figure 2. Top: SC light curve for Kepler-71, Transit 3. The solid line is the data smoothed every 10 points. Bottom: Residuals after subtraction of a spotless model (red curve in top panel). Potential starspot and facula signatures are centred at approximately 0 h, -1.0 h, and + 0.8 h, respectively, from transit centre, as indicated by the black arrows. The time at transit centre corresponds to transit epoch 547.3541 BKJD (Barycentric Kepler Julian Date, BJD-2454833). The spot and faculae signals are detected beyond the rms noise (dotted horizontal line). The vertical dashed lines mark the beginning of ingress and egress of the planet on to the stellar disc.

(Berdyugina 2004). We find the presence of both starspots and faculae on Kepler-71, as shown in Fig. 2.

The model represents the stellar surface as a two-dimensional pixelated white light image (disc) with varying intensity, I, decreasing with $\mu = \cos(\theta)$, where θ is the angle between the line of sight and the emergent intensity. The quadratic limb darkening applied to the image is given by

$$\frac{I(\mu)}{I_c} = 1 - u_1(1-\mu) - u_2(1-\mu)^2 \quad (1)$$

where I_c is the maximum intensity at disc centre, and u_1 and u_2 are the limb darkening coefficients.

The planet is a dark, opaque disc with a radius defined in units of the stellar radius. Its orbit is calculated given the physical parameters of the host star-exoplanet system, specifically the semimajor axis and inclination angle of the planet's orbit. The planetary orbit is assumed to be circular, given the lack of RV data to otherwise constrain the eccentricity value. The angle between the orbital and stellar spin axes may be input for oblique transits. However, for the Kepler-71 system, the transit latitude remains unchanged between transits, and thus, the orbit is adopted as coplanar with the stellar equator. The presence of the same magnetic features on consecutive transits infers an obliquity close to zero. The model determines the orbital position of the planet every two minutes, and the stellar intensity is calculated by summing over all pixels in the stellar image. This technique produces a noiseless, or unspotted, transit light curve as a function of time.

The parameters used to model the noiseless transit light curve include orbital semimajor axis, inclination, planet radius, planet orbital period, and quadratic limb darkening coefficients. A preliminary model light curve is generated using parameter values available in the literature. To ensure that the shape of the transit is well described by the parameters, the model is fit to an average of the normalized and phase folded observed transits. A first fit of the published values for semimajor axis, planet radius, inclination, and quadratic limb darkening coefficients was performed using the χ^2 minimization routine AMOEBA (Press et al. 1992). The resulting fit parameters where then used as initial values to a Monte Carlo Markov Chain (MCMC) ensemble sampler. We chose to run an IDL version of the affine-invariant ensemble sampler for MCMC's proposed by Goodman & Weare (2010) and introduced in PYTHON by Foreman-Mackey et al. (2013). By sampling from a posterior probability representing a distribution of parameters consistent with the observed data, we obtained the most probable parameters and their uncertainties. Given the limited number of parameters input to the transit model, it was sufficient to calculate likelihoods and posterior probabilities for thousands of walkers and thousands of iterations of the Goodman & Weare MCMC sampler (GWMCMC). The walkers stretched through the parameter space during a relatively short burn-in phase. All GWMCMC chains were flattened before splitting the walker values for each starspot and facula parameter into confidence intervals using quantiles of 16 per cent, 50 per cent, and 84 per cent. Each parameter value was accepted as the median (50 per cent) value of its sampling, with lower and upper 1σ errors corresponding to the 16 per cent and 84 per cent quantiles (Hogg & Foreman-Mackey 2018).

As required by unbiased sampling, prior knowledge of the transit model parameters was not assumed. The parameters were allowed to explore parameter space freely but within physically acceptable bounds set by uniform priors. The priors are given in Table 2. To remove any degeneracy with other parameters, the limb darkening coefficients were parametrized following the triangular sampling methodology of Kipping (2013). At each iteration of the sampler, the parametrized coefficients were re-expressed as u_1 and u_2 before calculating the model transit light curve.

The optimized transit model parameters are given in Table 1. To best fit the averaged transit shape, the semimajor axis increased by 4.5 per cent, the inclination increased by 4.5 per cent, and the planet's radius decreased by 3.2 per cent. Limb darkening coefficient 1 decreased and limb darkening coefficient 2 increased from previously published values.

Secondary transit parameters, which include impact parameter, transit latitude, and transit duration, are computed from the fit parameters and are given in Table 3. Impact parameter and transit latitude are determined by inclination angle and semimajor axis, as

Table 2. Uniform priors for model light curve fitting.

Parameter	Range
Planet radius (R_{star})	[0.02–0.2]
Semimajor axis (R_{star})	[9–16]
Inclination angle (°)	[85–95]
Impact parameter	[0.01–0.5]
Parametrized limb darkening coeff 1	[0–1]
Parametrized limb darkening coeff 2	[0–1]

Table 3. Secondary transit parameters of the Kepler-71 system.

Parameter	Value
Transit latitude (°)	$-5.404\ ^{+0.003}_{-0.007}$
Impact parameter	0.0942 ± 0.0001
Transit duration (h)	2.771 ± 0.001

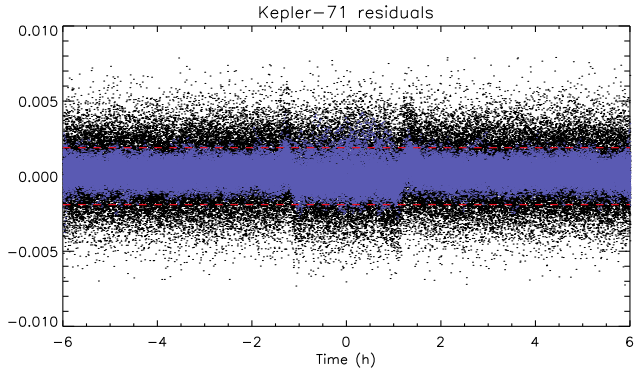

Figure 3. Residuals of all *Kepler* SC transit light curves. The black dots are the residuals for all observed light curves after subtraction of the transit model constructed using optimized parameters. The blue dots are the same data smoothed every 10 points. The horizontal red lines represent the unsmoothed out-of-transit rms.

given by

$$b = \frac{a\cos(i)}{R_{\rm star}} \tag{2}$$

$$lat_{\rm tran} = \arcsin\left[\frac{a}{R_{\rm star}\cos(i)}\right] \tag{3}$$

where a is the semimajor axis, $R_{\rm star}$ is the stellar radius, and i is the inclination of the planet's orbit. We have arbitrarily chosen the transit projection to be in the Southern hemisphere.

Though the light curves have been pre-conditioned, they remain inherently noisy with possible contributions from long-term stellar variability or instrumental effects. The residuals for all observed light curves after subtraction of the model constructed with the parameters obtained from the GWMCMC fit are shown in Fig. 3 as black dots. The blue dots are the same data smoothed every 10 points. The red horizontal lines banding the smoothed data represent the unsmoothed out-of-transit rms, which is approximately ten times the 3 h Combined Differential Photometric Precision (CDPP; Christiansen, Jenkins & Caldwell 2012) of 184 ppm. The calculated rms noise of the unsmoothed residuals is 0.0020 in-transit and 0.0019 out-of-transit. After smoothing the residuals every 10 points, the rms noise is reduced to 0.00063 out-of-transit and 0.00093 in-transit. The in-transit rms is greater than the out-of-transit rms in both cases, indicating the presence of magnetic features. The smoothed data will be used in the search for stellar activity signatures (see Section 4).

The optimized light curve simulating a transit across the unspotted stellar disc is compared to each observed transit light curve to disclose the presence of surface variations. When the transited stellar surface contains starspots or faculae, a modulation beyond the typical irregularity due to stellar noise is seen in the flux residuals resulting from subtraction of the light curve model from observed light curve data. Bumps and dips in the residuals indicate the position of starspots and faculae, respectively, as a function of time (see bottom panel of Fig. 2).

Estimates of starspot and faculae physical characteristics may be added to the unspotted model in order to synthesize spotted light curves. We define a spotted light curve as one which includes modulations due to starspots only, faculae only, or starspots and faculae. Starspots and faculae are modelled as discs with three free parameters: radius, intensity, and longitude. Starspot and facula

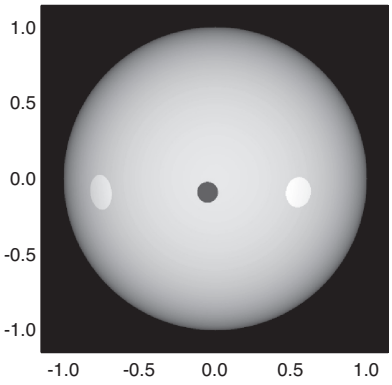

Figure 4. 2D representation of the limb darkened surface of Kepler-71 with one starspot (black) and two faculae (white) inferred from Transit 3 features.

latitudes are that of the projected planetary transit on the surface of the star, which for Kepler-71b is -5.4°, close to the stellar equator given an orbital inclination of 89.56°.

Radius and intensity may be inferred from the width and amplitude of modulations. Longitude is calculated from the estimated time at the centre of a modulation. Starspot/facula longitude is defined relative to the stellar topocentric longitude, 0°, which is the centre of the projection of the planet on to the stellar disc at mid-transit ($t = 0$). Longitudes are constrained to $\pm 80^\circ$ of disc centre to avoid measurement inaccuracies caused by the steep variations in intensity during ingress and egress, i.e. near the limb (Silva-Valio et al. 2010). Longitude is converted from transit time to stellar longitude by

$$\mathrm{lon}_{\rm spotfac} = \arcsin\left[\frac{a\cos\left(90^\circ - \frac{360^\circ}{24}\frac{t_s}{P_{\rm orb}}\right)}{\cos(\mathrm{lat}_{\rm tran})}\right] \tag{4}$$

where a is the semimajor axis, $P_{\rm orb}$ is the orbital period, $\mathrm{lat}_{\rm tran}$ is the transit latitude, and t_s is the time at bump maximum height or dip maximum depth.

Starspots and/or faculae are modelled for each observed transit of Kepler-71 having the signatures of magnetic activity. The number of starspots and faculae added to the model noiseless light curve can vary per transit. For the majority of transits, we found that a maximum of four magnetic features per transit could be distinguished from noise and added to an unspotted model. The unspotted model is visually compared to each observed transit, and the flux residuals remaining after subtraction of the spotless model from observed data are compared to the transit noise to verify that starspot and facula signatures are discernable from the noise (see discussion in Section 4.1). For those transits having starspot and/or facula modulations that pass our selection criteria (discussed in Section 4.1), estimates for those modulations are added to the unspotted model on a per transit basis to create a spotted light curve unique to each observed transit. An example of the 3rd transit of Kepler-71 is given in Fig. 2. The top panel depicts the observed transit, smoothed every 10 points, with an overlay of the unspotted transit model in red. As shown in the bottom panel, the residuals obtained when subtracting the unspotted model from the observed light curve indicate magnetic features that are distinct from the noise. Estimates for the radius, intensity, and longitude of each feature are added to the unspotted model to build a spotted model. A two-dimensional representation of the stellar surface is given in Fig. 4. The dark starspot and two bright faculae are pictured on a limb darkened simulation of the stellar surface.

Table 4. Uniform priors for starspots and faculae.

Parameter	Value
Starspot	
Radius (R_{planet})	[0.2, 2.0]
Intensity	[0, .99]
Longitude	[−80, 80]
Facula	
Radius (R_{planet})	[0.2, 2.0]
Intensity	[1.01, 1.50]
Longitude	[−80, 80]

For each starspot and facula, the radius is defined in units of planetary radius R_p, and the intensity is constrained from 0 to less than 1 for starspots and from greater than 1 to 1.5 for faculae [in units of central stellar intensity I_c ($\mu = 1$)]. Initial fit starspot and facula parameters are set to mid-range values for radius and intensity, 1.0 R_p and 0.5 I_c ($\mu = 1$) for starspots and 1.0 R_p and 1.25 I_c ($\mu = 1$) for faculae. Initial fit longitude at the centre of each magnetic feature is estimated by equation (4) above. Starspot and facula physical characteristics are added to the unspotted model light curve at their estimated central longitudes. Best fit of the observed and synthesized spotted light curve for each transit was performed using GWMCMC. Starting with initial values for starspot and/or facula parameters, GWMCMC simultaneously optimized the three degrees-of-freedom (radius, intensity, and longitude). The uniform priors for the parameters are given in Table 4. The GWMCMC sampling yielded median values for starspot/faculae parameters from which high probability spotted light curves unique to each magnetically active transit can be synthesized.

4 RESULTS

Assuming solar-type activity, we anticipated both the presence of starspots at longitudes along the transit chord from the central meridian to the stellar limbs and the observation of faculae closer to the stellar limbs. Yet, many bright regions were discovered along the transit chord away from the stellar limb.

Magnetic activity, such as starspots and/or faculae, was observed in several of the 117 complete transits for Kepler-71. For many transits with magnetic activity, the out-of-transit noise was equal to or greater than the in-transit flux residuals resulting from subtraction of an optimized model light curve. Thus, the noise masked many starspot and facula signatures and reduced the number of identifiable starspots and faculae. Light curves were examined over a span of ±6 h from mid-transit time (= 0) to compare out-of-transit flux changes to those within the transit, which has a duration of 2.77 h.

Given that the stellar rotation rate and planetary orbital period are in an approximate 1:5 resonance, transit light curves in sequences of every fifth transit were analysed to accentuate any starspot and/or facula signatures. The light curves from transits 186, 191, 196, and 201 are shown as the top four curves in Fig. 5. The transit epoch in BKJD at mid-transit is included, indicating the five orbital period intervals of approximately 19.5 d between transits.

The light curves within the transit, bounded by the vertical solid lines in Fig. 5, show two magnetic features, a starspot at time 0.5h and a faculae at −0.5 h (times refer to the bottom transit shown in black with centre at 1320.5597 BKJD). Since the noise of transit data is significant, the light curves of the four transits were averaged to accentuate the features. As the rotation period of the star is slightly larger than five times the planetary orbital period, each transit had to be shifted in time by 0.06 h accordingly. The displacement corresponds to a stellar rotation period of 19.71 d at the transit latitude. Thus, the dashed lines indicating the starspot and facula appear somewhat slanted. The averaged light curve after the time correction is shown as bottom curve of the figure. As can be seen, the noise outside the transit decreased by a factor of 2 while the two features remained.

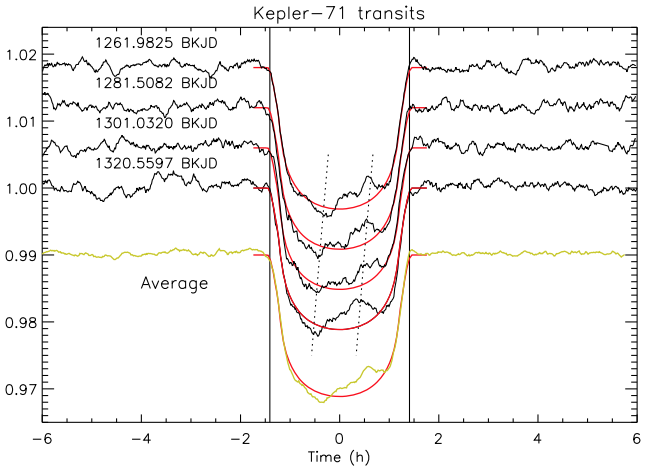

Figure 5. In black, light curves for a sequence of every fifth transit in descending order: Transit 186, Transit 191, Transit 196, and Transit 201, with mid-transit time of each transit given in BKJD. The solid red curves represent the model transit of an unspotted star. The vertical lines mark ingress and egress. The bottom curve (yellow) is an average of all four transits after each is shifted by 0.06 h. The slanted dashed lines cross the positions of a starspot and a facula in the four transits.

The starspot and the facula proved to be occulted during 15 consecutive planetary rotations. Due to their persistence, these magnetic features were accepted as confirmed. Their lifetimes are at least 60 d.

4.1 Modelling starspots and faculae

We visually compared each of the transit light curves of Kepler-71 to an overlay of the model light curve to search for indications of starspots/faculae. For those transits showing potential magnetic variations, the residuals resulting from the subtraction of the GWMCMC optimized model transit light curve from observed transit data were evaluated. Residuals indicating starspots and/or faculae had to meet one the following criteria before being fit via GWMCMC to obtain values for starspot/facula radius, longitude, and intensity: (1) residuals exceed ±100 per cent of the unsmoothed out-of-ransit rms, (2) residuals meet or exceed ±66 per cent of the rms with overall transit noise within ±66 per cent of the rms, or (3) residuals meet or exceed ±66 per cent of the rms and the magnetic feature(s) is(are) repeated every fifth transit.

Fig. 6 for Transit 34 depicts examples of the transit light curve with an overlay of the model and the flux residuals as compared to ±66 per cent and ±100 per cent of the rms. This figure also illustrates the noise in the observed light curves and the difficulty of discerning magnetic features from that noise. The upper panel shows flux variations in the observed light curve when compared to the model light curve. There appear to be a starpots at $t = -0.75$ and a facula at $t = 0.8$ h.

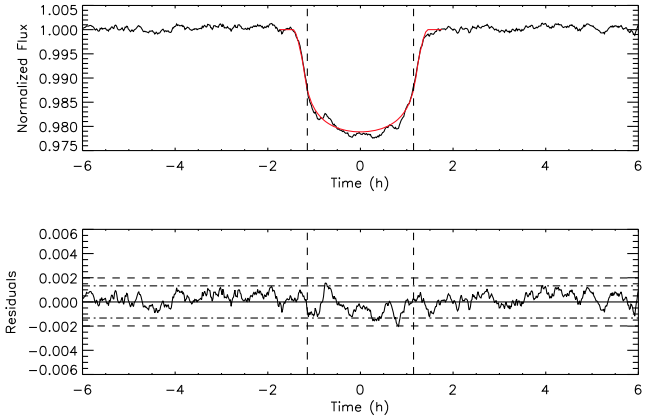

Figure 6. *Top:* Example of the light curve for Transit 34 (transit epoch 668.4125 BKJD) with a starspot at t = -0.75 h and a facula at t = 0.8 h. The smooth, u-shaped curve represents a spotless model. The vertical dashed lines highlight the area of interest. *Bottom:* Residuals after the subtraction of the spotless model from the transit light curve. The dot-dashed lines represent ±66 per cent of the unsmoothed out-of-transit rms, whereas the dashed lines represent ±100 per cent of the unsmoothed out-of-transit rms.

Table 5. Transit distribution of starspots and faculae.

Magnetic feature	No. of transits	Singlet	Doublet	Triplet	Quadruplet
Starspots and faculae	21	0	10	9	2
Starspots only	34	21	13	0	0
Faculae only	17	8	9	0	0

Singlets are defined as only one starspot or facula per transit. Doublets are defined as either two faculae, two starspots, or one starspot and one facula per transit. Triplets are defined as either one starspot and two faculae or two starspots and one facula. Quadruplets are defined as two starspots and two faculae or three starspots and one facula.

The flux residuals in the lower panel of Fig. 6 are plotted against both ±66 per cent and ±100 per cent of the unsmoothed out-of-transit rms. When applying the above criteria, the starspot at -0.75 h and the facula at 0.8 h fail to meet criteria 1, having residuals just below ±100 per cent of the rms. The residuals do, however, pass criteria 2 since they are between ±66 per cent and ±100 per cent of the rms and the out-of-transit noise is well contained within ±66 per cent of the rms. Criteria 3 can only be applied successfully to the spot residual since it meets the rms requirement and reappears in a sequence of every fifth transit at a temporally shifted position.

Magnetic features that either met an out-of-transit rms threshold for individual transits or were occulted during consecutive planetary rotations were modelled as described in Section 3. In total, 76 starspots and 52 faculae were identified in the observed transit light curves and modelled using GWMCMC. Of the 21 transits with a starspot-facula doublet, triplet, or quadruplet, 13 transits had starspot-faculae adjacent pairs. The remaining starspots and faculae were spatially separated. Twenty-nine transits contained a single starspot or facula. Nine transits had just 2 faculae, and 13 transits had only 2 starspots. The distribution of starspots and faculae among the 72 transits is summarized in Table 5.

Histograms of starspot and facula physical parameters are given in Fig. 7. Mean starspot radius is 0.61 ± 0.32 R_p, or (51 ± 26) × 10^3 km. Starspot radii fall within the range of 0.24–1.66 R_p, or (20–138) × 10^3 km. Mean starspot intensity is 0.55 ± 0.23 I_c, where $I_c(\mu = 1)$ is the central intensity of the photosphere. Starspot intensity falls within the range of 0.01–0.92 I_c. Starspot longitudes span −80° to 57°, where 0° longitude corresponds to the central meridian of Kepler-71 at mid-transit in the reference frame of the observer on Earth. As can be seen from the longtiude histogram, the spots longitude distribution is bell shaped and centred around zero longitude.

The mean facula radius is 0.80 ± 0.31 R_p, equivalent to (67 ± 25) × 10^3 km, 31 per cent larger than the mean starspot radius. Facula radii fall within the range of 0.42–1.98 R_p, or (35–165) × 10^3 km. Mean facula intensity is 1.19 ± 0.09 I_c. Facula intensity falls within the range of 1.08 to 1.50 I_c, with intensity greatest towards the stellar limb. Facula longitudes span −58° to 64°. As compared to the spots longitude distribution, the faculae longitude distribution is not centred about zero longitude, with many faculae closer to the stellar limb. Spots are more concentrated towards the centre of the stellar disc, whereas the faculae tend to occur closer to the limb with peaks in the distribution around ±50°. This behaviour is similar to that observed for solar faculae.

The area coverage of the magnetic features was estimated considering the radius of starspots and faculae and the total stellar area occulted by the planet during its transit. The results are plotted in Fig. 8. The starspots (red histogram) occupy about 4.3 per cent of the area of the transit latitudes, approximately two thirds the area occupied by faculae (black histogram). Thus, the average ratio of the faculae to spot area, Q, is 1.7, which is smaller than that for the Sun (Q = 9; Lanza 2010). However, solar-like stars that are more active than the Sun have typically smaller contribution from the facular area: Q = 1.5 for CoRoT-2 (Lanza et al. 2009a) and CoRoT-6 (Lanza et al. 2011), Q = 1.6 for Kepler-17 (Bonomo & Lanza 2012), and Q = 4.5 for CoRoT-4 (Lanza et al. 2009b).

To further evaluate the effective brightness of faculae along the transit chord, facula intensity was converted to flux using the following equation

$$F_{fac} = r_{fac}^2(I_{fac} - 1), \quad (5)$$

where r_{fac} and I_{fac} are facula radius and intensity, respectively.

Similarly, the starspot flux can be estimated by

$$F_{spot} = r_{spot}^2(1 - I_{spot}), \quad (6)$$

where r_{spot} and I_{spot} are spot radius and intensity, respectively.

The flux values, in arbitrary units, with longitude for both starspots (red diamonds) and faculae (black asterisks) are plotted in the bottom panel of Fig. 9. As can be seen in the figure, facula flux surplus increases towards the limb more prominently than the spot flux deficit. The trend significantly steepens for longitudes larger than ±45°, indicating a solar-like trend. The starspot flux does not follow a strong increase in value with longitude, as would be expected.

The intensity of the 52 modelled faculae is shown in the top panel of Fig. 9. The solid black line is a model for the increase of solar faculae intensity towards the limb given by $1 + c_f(1 - \mu)$, where $\mu = \cos(\theta)$ is the cosine of the heliocentric angle and c_f = 0.115 to represent the increase of solar faculae at the limb. The blue line is this same equation with a factor of 0.2 in intensity added, showing that the Kepler-71 faculae, despite being brighter than the solar counterparts, follow a similar increase when seen closer to the limb. Thus, the faculae found on Kepler-71 are approximately 20 per cent brighter than their solar counterparts near disc centre.

Criscuoli, Norton & Whitney (2017) studied the photometric properties of network and faculae observed on the Sun using restored images from the Helioseismic Magnetic Imager. For the purposes of their study, magnetic features were classified by their distance from active regions. They found that the network exhibits

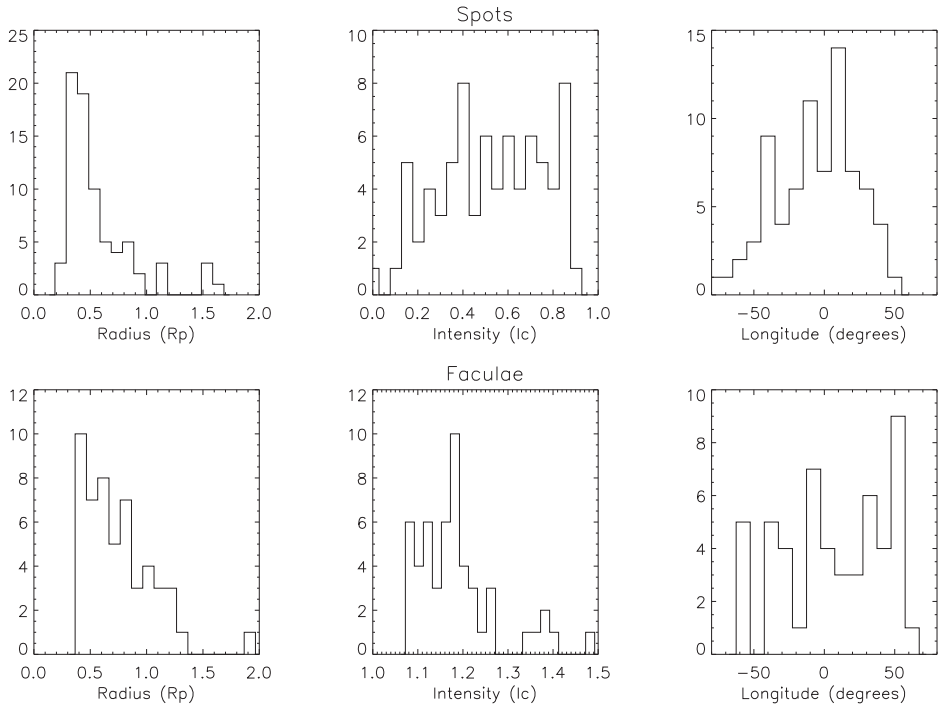

Figure 7. Histograms of starspot (top row) and facula (bottom row) physical parameters (from left to right): radius, intensity, and longitude.

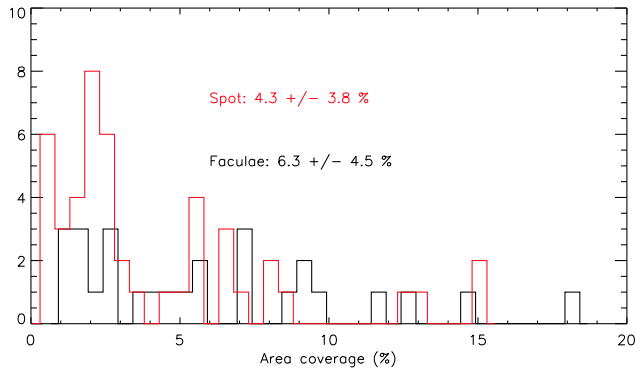

Figure 8. Histograms of the area coverage of starspots (red) and faculae (black). The inset values are the relative areas occupied by starspots and faculae at the transit latitude band.

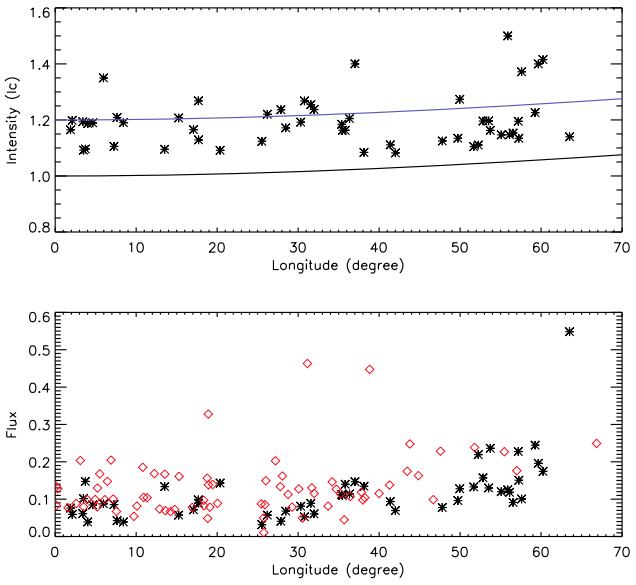

Figure 9. Top: Faculae intensity with longitude. The solid black line represents the dependence of solar facula intensity on heliocentric angle, whereas the blue line is this model with an extra 0.2 added for the case of Kepler-71. Bottom: Facula (black asterisk) and spot (red diamond) fluxes as a function of stellar topocentric longitude.

higher contrasts than faculae, with contrast differences smaller towards disc centre and increasing towards the limb. The contrast is especially high for magnetic flux larger than 300 G, being twice as much for features close to the limb.

Kobel, Hirzberger & Solanki (2018) concur that faculae contrast increases towards the limb but differ as to the contrast near disc centre. Using *G*-band and G-continuum filtergrams from the 1m-Swedish Solar Telescope, they evaluated the properties of photometric features classified as bright points or faculae with respect to heliocentric angle and found that the centre-to-limb variations for both bright points and faculae is non-zero at disc centre and increase with an equivalent trend towards the limb. While the orientation of faculae towards the limb were radial, the orientation near disc centre showed a varied distribution in direction, indicating a hot wall effect induced by inclined fields. Such fields would produce an inclined view of the facular wall. We propose that the faculae observed on Kepler-71 near disc centre are due to very strong and/or inclined magnetic fields.

4.2 Rotation period at the transit latitude

The movement of starspots in and out of the observer's view with stellar rotation has been used to measure the stellar rotation rate

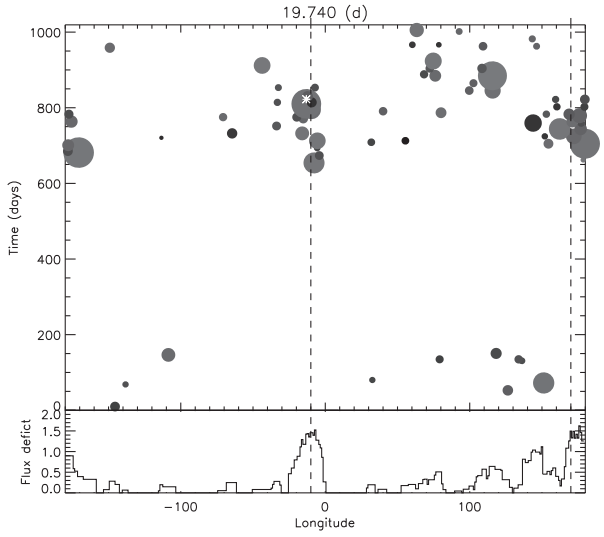

Figure 10. Top: A spot map of the stellar surface with time, i.e. the location of spot longitudes in the rotating frame of the star (with a latitudinal rotation period of 19.74 d) for all transits. The size of the circles represents starspot radius. The spot marked by asterisks is discussed in Section 4.3. Bottom: The total flux deficit caused by the spots. The dashed vertical lines are 180° apart in longitude and roughly indicate the maximum of the spot flux deficit.

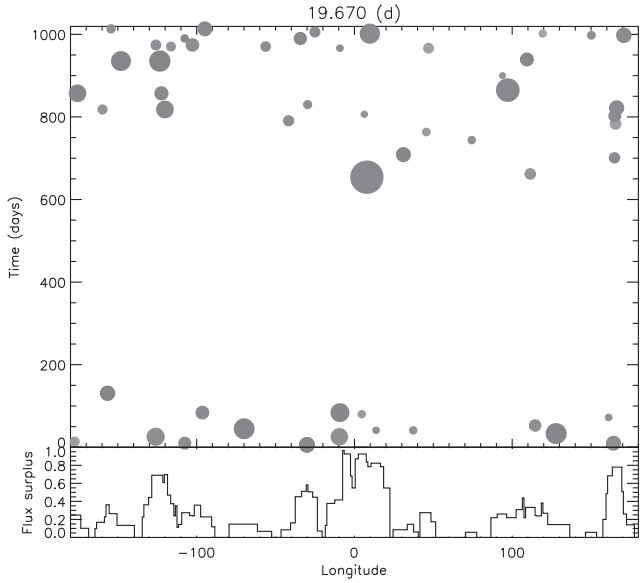

Figure 11. Same as Fig. 10 but for faculae with a stellar rotation period of 19.67 d at the transit latitude. Bottom: Faculae excess flux as a function of longitude.

at the transit latitude and estimate the stellar surface differential rotation (Silva-Valio & Lanza 2011; Valio 2013; Netto & Valio 2016; Valio et al. 2017). The procedure used in those studies employed autocorrelation of flux deficit, the intensity difference due to the presence of spots at different longitudes, to determine stellar rotation rate at the transit latitude. The period was taken as that which corresponded to the autocorrelation function (ACF) with the smallest FWHM.

To estimate the stellar rotation period at the transit latitude, we first considered the 76 starspots identified for all transits. The FWHM of the ACF of the flux deficit caused by the presence of the spots calculated for several latitudinal rotation periods yields a rotation period of 19.74 ± 0.05 d. This rotation period corresponds to the minimum width and is, thus, assigned to the rotation period of the star at latitude −5.4° as far as starspots are concerned. Once the stellar rotation period at the transit latitude band has been calculated, a map of the spot locations in time may be built. Such a map is shown in Fig. 10 for $P_{\rm star}$ = 19.74 ± 0.05 d. Starspot longitudes have been converted from the topocentric coordinate system to one that rotates with the star. The difference in flux estimated by equation (6) is shown in the bottom panel.

The same calculation was performed for the 52 observed faculae. The result is shown in Fig. 11. In this case, the autocorrelation of the flux surplus reaches a minimum at a rotation period of 19.67 ± 0.05 d. The flux surplus estimated by equation (5) is shown in the bottom panel.

The rotation periods estimated here agree with that obtained from the tracking of a facula and a starspot identified in every fifth transit shown in Fig. 5. For these magnetic features to be displayed on the same longitude after five transits, displacements commensurate with a rotation period of 19.71 d were added. Hence, we adopt a latitudinal rotation period of 19.71 d from the mean of the rotation periods calculated for starspots and faculae.

4.3 Obliquity

Since we are detecting the same features in later transits, the obliquity must be very small. However, we cannot use the data from transits five periods apart due to the 1:5 resonance, since the same hemisphere of the star will be facing Earth every five orbital periods, which is approximately $P_{\rm star}$. On the other hand, the fact that we see the same feature on a later transit that is not a multiple of five does prove that the obliquity is close to zero.

To estimate its maximum value, we can use the position of a spot identified on two consecutive transits (208 and 209) at longitude −13° in the frame that rotates with the star, marked by asterisks on Fig. 10 (both spots are overlaid and cannot be discerned in this figure due to the vertical scale). However, as seen from Earth, the topocentric longitudes are −29.5° and +41.8° for transits 208 and 209, respectively. These transits are plotted in Fig. 12 with the spot signatures marked by dashed vertical lines and separated by about 1.4 h, which corresponds to 71°. During each planetary orbit, the star rotates $360^\circ P_{\rm orb}/P_{\rm star} = 71^\circ$.

The planet radius, $R_{\rm p}$, is $0.1358\,R_{\rm star}$, and so the planet eclipses about $2\,R_{\rm p}\,90^\circ \sim 24.5^\circ$ in latitude. In the extreme case that the bottom half of the spot is eclipsed in the bottom transit of the figure and then the top half of the spot is eclipsed in the top transit, we have for the obliquity, Ψ:

$$\Psi = \arctan(24.5/431) \sim 3^\circ. \quad (7)$$

Thus, the obliquity of the planet orbit in this case is less than 3°.

4.4 Average rotation period and active longitudes

The rotation period of the star can be determined from the modulation seen in the light curve of the star as dark spots and bright faculae rotate in and out of view. However, this will be an average period since the star rotates differentially. This average rotation period can be estimated from the out-of-transit light curve.

To confirm the mean stellar rotation period of 19.77 d obtained previously by McQuillan et al. (2013), we applied the autocorrelation technique for period detection described in McQuillan et al.

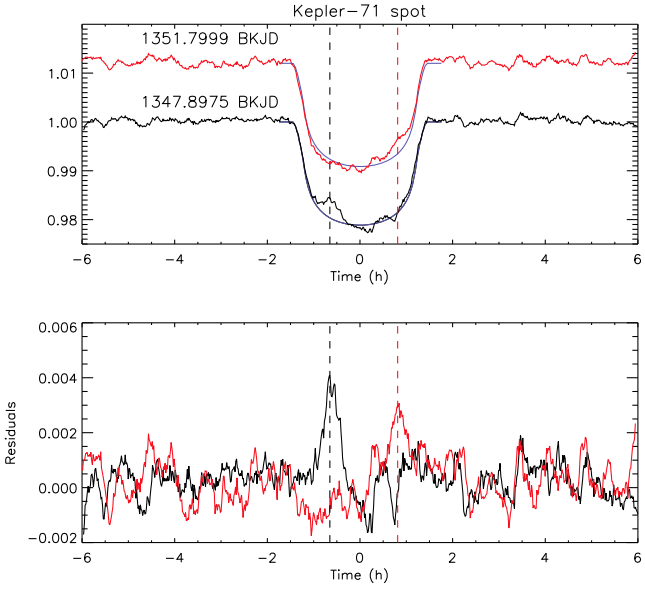

Figure 12. Top: Repeat presence of a spot in two consecutive transits, as indicated by the dashed vertical lines. The bottom light curve is Transit 208 (black curve), whereas the top curve is consecutive Transit 209 (red curve). Mid-transit time is given in BKJD. The solid curve is an unspotted model. Bottom: Residuals after subtraction of the spotless model from the transit light curves, The vertical lines mark the spot signatures in the residuals for Transits 208 and 209. The temporal separation of the occurrences of the spot is 1.4 h or approximately 71°.

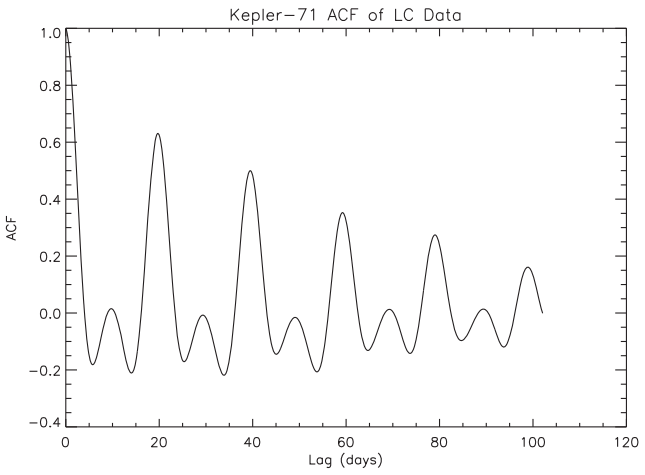

Figure 13. ACF of LC data for Quarters 3–16 after removal of transits. The series of high peaks indicate the stellar rotation period, while the series of low peaks reflect a secondary period possibly due to opposing active longitudes.

(2014) to LC data for Quarters 3–16. McQuillan et al. (2013) utilized the light curves from Quarters 3–14 to arrive at a rotation period of 19.768 ± 0.096 d. We additionally considered the data from full Quarters 15 and 16 but did not include the data from Quarter 17 due to the early termination of that quarter caused by reaction wheel failure. All transits were removed from the LC data before normalizing each quarter and re-gridding the complete data set in continuous time-steps of 29.4 min. The output of the ACF is given in Fig. 13. The ACF clearly shows two distinct periods. The series of high peaks are indicative of the stellar rotation period, while the low peaks reflect a secondary period possibly caused by opposing active regions. The slopes of straight lines fit to the first four peaks for each period yield rotation periods of 19.773 ± 0.008 d and 9.92 ± 0.05 d. We are, thus, confident in a mean stellar rotation period of 19.77 d for Kepler-71.

The peak at 9.92 d is most likely a harmonic of the stellar rotation frequency that corresponds to the 19.77 d period. Such a harmonic may occur when there are active longitudes on the surface of the star, where spots tend to appear, separated by 180° degrees in longitude.

To search for active longitudes on the surface of the star, we examined the stellar surface maps at the transit latitude for both magnetic features, starspots and faculae (Figs 10 and 11). The spot map in Fig. 10 indicates the presence of active longitudes. To guide the eye, vertical dashed lines have been drawn roughly matching the peaks in flux deficit . The flux deficit peaks at approximately -10° and 170°, displaced by 180°. Thus, we confirm the second peak in the ACF at 9.92 d.

4.5 Differential rotation

All the stellar rotation periods calculated above at latitude −5.4° are shorter than the out-of-transit period of 19.77 d. Assuming that the rotational profile is similar to that of the Sun, we calculated the differential rotation of Kepler-71 by fitting the estimated latitudinal rotation period to a solar profile. Differential rotation of the Sun is described by the following simplified solar law.

$$\Omega(\alpha) = \Omega_{\rm eq} - \Delta\Omega\ \sin^2(\alpha), \tag{8}$$

where Ω is the angular velocity, $\Omega_{\rm eq}$ is the equatorial angular velocity, $\Delta\Omega$ is rotational shear, or the difference in angular velocity between the equator and pole, and α is stellar latitude.

Assuming a similar profile for Kepler-71, the equatorial angular velocity and rotational shear can be estimated by fitting a generic differential rotation profile.

$$\Omega(\alpha) = A - B\ \sin^2\alpha \tag{9}$$

where A and B are the stellar equatorial angular velocity and rotational shear, respectively.

The average rotation is obtained by integrating equation (9) from the minimum latitude to the maximum latitude where spots (or faculae) emerge.

$$\bar{\Omega} = \frac{1}{(\alpha_2 - \alpha_1)} \int_{\alpha_1}^{\alpha_2} \left(A - B\ \sin^2\alpha\right) {\rm d}\alpha, \tag{10}$$

where α_1 and α_2 are the minimum and maximum latitudes, respectively. For the Sun, we can assume that spots emerge from latitudes near the equator to a maximum of ±35°. Young stars have spots all the way to the poles, i.e. from 0° to 90° latitudes.

Thus we have two equations, given by the rotation at the transit latitude (equation 9) and the average out-of-transit rotation (equation 10), and two unknowns, A, the rotation at the equator, and B, the shear. Considering that the minimum latitude of spot (or faculae) occurrence is the equator, we now have to estimate the maximum latitude for the magnetic features.

Similar to the Sun, the emergence of starspots on Kepler-71 should replicate the butterfly trend of sunspots, appearing within latitude bands on either side of the solar equator. The rotation of stars younger than the Sun with shorter rotation periods will produce a Coriolis force that deflects flux tubes to higher latitudes (Granzer 2004). The mean stellar rotation period of Kepler-71 is approximately 75 per cent of that for the Sun, and thus, the maximum emergence latitude of spots on Kepler-71 will be greater than

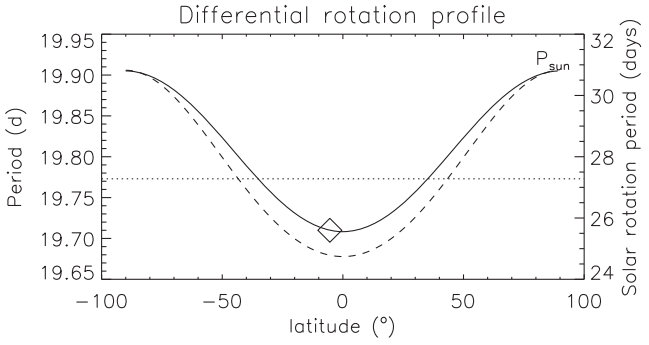

Figure 14. Differential rotation profiles for Kepler-71 (solid line) and the Sun (dashed line). The diamond represents the period of 19.71 d at latitude −5.4° found from temporal starspot and facula mapping.

solar. For a star with equivalent solar mass, the maximum emergence latitude will be ±65°.

The differential rotation profile we generated for Kepler-71 over the latitude range [0.0°, 65.0°] using the mean stellar rotation period of 19.71 d at the transit latitude of −5.4° is depicted in Fig. 14. The diamond marks the profile location for transit latitude −5.4° and rotation period 19.71 d. Considering the rotation of 19.74 d obtained from spots, we calculate a rotational shear of $\Delta\Omega = 0.0015 \pm 0.0025$ rad d^{-1} and a relative differential rotation of $\Delta\Omega/\bar{\Omega} = 0.5 \pm 0.8$ per cent, where $\bar{\Omega} = 2\pi/P_{\rm star}$ and $P_{\rm star}$ is the out-of-transit mean stellar rotation period of 19.77 d. If we consider the slightly smaller rotation period obtained from faculae only, 19.67 d, the shear is $\Delta\Omega = 0.0052 \pm 0.0025$ rad d^{-1} with a relative differential rotation of $\Delta\Omega/\bar{\Omega} = 1.6 \pm 0.8$ per cent. Hence, Kepler-71 star apparently has very little differential rotation.

5 DISCUSSION

Kepler-71b is a hot Jupiter orbiting a solar-type G-star younger than the Sun. The mean stellar rotation period of Kepler-71 at 19.77 d is consistent with that of a G-class star somewhat younger than the Sun (Guinan & Engle 2009). Rotational evolution of main-sequence stars is closely related to changes in angular momentum. In particular, the proximity of hot Jupiters to their host stars contributes to significant angular momentum loss in G-type stars and as such affects the early evolution of stellar rotation (Lanza 2010). The orbit of a hot Jupiter through the closed magnetic field lines of the stellar corona of its host star induces a greater loss of angular momentum through coronal mass ejections rather than through a magnetized wind. As a star ages and slows, the effect of the hot Jupiter may not be as impactful. The current rotation rate of Kepler-71 may be assigned to early coronal mass eruptions followed by angular momentum loss through stellar winds. Lanza (2010) observed trends in the synchronization of stellar rotation and planetary orbit relative to stellar effective temperature. For cool stars with $T_{\rm eff} < 6000$ K, the stellar rotation period is much longer than the planetary orbital period, and the spin–orbit synchronization ratio can be as great as 1:6 (Lanza 2010). Kepler-71 is a cool star at $T_{\rm eff} = 5540$ K. The synchronization ratio of the Kepler-71 system is approximately 1:5, given a mean stellar rotation period of 19.77 d and planetary orbital period of 3.91 d, and exemplary of the trend observed by Lanza.

The photometric variations of Kepler-71 are characteristic of a solar-type star with an internal magnetic dynamo driven by the interplay of stellar rotation and plasma convection. We have estimated the stellar rotation period and derived therefrom differential rotation of Kepler-71 at the transit latitude of −5.4° by mapping the positions of faculae and starspots along the transit chord. The stellar rotation period at the transit latitude, as determined by the longitudinal change in position of faculae, is 19.67 ± 0.05 d, slightly smaller than the mean stellar rotation period of 19.77 d. Further, the value for differential rotation from faculae is supported by the differential rotation derived from the mapping of starspots. The stellar rotation period calculated from the longitudinal movement of starspots yields a rotation period of 19.74 ± 0.05 d, again less than the mean stellar rotation period of 19.77 d. Thus, the rotation period from faculae and that from starspots are complementary, differing by less than 1 per cent. Given the latitudinal rotation periods derived for faculae and starspots, we calculate a rotational shear bounded by $\Delta\Omega = 0.0015$ and 0.0052 rad d^{-1} and a relative differential rotation within $\Delta\Omega/\bar{\Omega} = 0.5$ per cent and 1.6 per cent.

The rotational shear of Kepler-71 is significantly smaller than the solar value of 0.055 rad d^{-1} (Berdyugina 2005) and indicative of likely rigid body rotation. Recent stellar models, e.g. the Küker & Rüdiger (2011) models, predict the variation of rotational shear with temperature but are lacking to predict the relationship between shear and rotation rate for G-stars (Balona & Obedigamba 2016). Observational data differs from predicted values. Reinhold et al. (2013) calculated the differential rotation of *Kepler* stars by associating Lomb–Scargle periods from light curves of different *Kepler* quarters with a secondary period being within 30 per cent of the primary rotation period. Assuming that changes in stellar rotation period are due to the appearance of starspots at differing latitudes between quarters, Reinhold et al. (2013) computed differential rotation values for more than 18 000 stars. Similar to the values presented by Barnes et al. (2005), the computations indicate a weak dependence of rotational shear $\Delta\Omega$ on rotation period and a slight increase in $\Delta\Omega$ over the temperature range $T_{\rm eff} = 3500$–6000 K. The values of rotational shear are bounded by the lower detection limit of 0.03 rad d^{-1} due to the subset of stars having only one detectable period. Instrumental effects of the *Kepler* telescope for slow rotators reduce the ability to detect a secondary period. Still, the values from Reinhold et al. (2013) demonstrate the weak correlation of rotational shear and rotation rate proposed by Küker & Rüdiger (2011), who modelled the rotational shear for Zero-Age Main-Sequence (ZAMS) stars of varying solar masses. From $T_{\rm eff} = 5400$–6800 K, there is a steady increase in rotational shear with temperature. At $T_{\rm eff} = 5500$ K, the predicted rotational shear is approximately 0.01 rad d^{-1} for a ZAMS star.

Unlike the photometric method of Reinhold et al. (2013), which is based upon the overall motion of magnetic features to set a lower limit on differential rotation, we have employed the technique of transit photometry mapping to characterize individual starspots and faculae and trace their positions along the transit latitude. We consider our value of differential rotation to be accurate though the result is lower than seen in other studies.

While the evidence for a rigidly rotating solar-type star younger than the Sun is perhaps surprising, various researchers offer physical mechanisms for this type of behaviour. Relatively rigid rotation may be attributed to processes that include angular momentum transport during Kepler-71's evolutionary development, planet–star interactions, or the generation of stresses in the convective zone. Adopting a model in which the radiative core and convective zones rotate at different rates as a result of angular momentum loss in the convective zone due to magnetized stellar winds, MacGregor & Brenner (1991) proposed that angular momentum transport in the stellar interior acts to redistribute angular velocity

at the tachocline. The time-scale during which angular momentum is transferred between the radiative core and convective zone, i.e. the core-coupling time-scale, and the amount of angular momentum exchanged affect the angular velocity gradients at the tachocline. A short coupling time-scale infers an efficient transfer of angular momentum, resulting in rigid body rotation (Bouvier 2013).

Kepler-71b is a hot Jupiter orbiting its host star at a distance of 0.047 au in a circular orbit. The planet and star each exert forces on its companion. In particular, the planet's gravitational potential generates a stellar tidal flow and may additionally be responsible for inertial waves in the convective zone. While the tidal force has been studied as to its effects on the evolution of the planet–star system structure, the effect of inertial waves on Sun-like stars and the interplay between internal stellar oscillation modes and differential rotation are new areas of investigation (Guenel et al. 2016).

The solar dynamo model states that magnetic fields generated at the tachocline are frozen in the convective zone plasma. The movement of the ionized plasma through the magnetic field creates electric currents. The magnetic field will in turn react back on the current flow through the Lorentz force. The reactive magnetic field may inhibit differential rotation (Ammler-von Eiff & Reiners 2012), resulting in lower measurements of differential rotation.

With respect to the large-scale electromagnetic fields, Varela, Strugarek & Brun (2016) propose that Maxwell stresses will decrease differential rotation due to their quenching effect on stellar magnetic fields. Varela et al. (2016) simulated the differential rotation of G and K solar-type stars of varying masses and rotation rates under the effect of magnetic fields and found that the interplay of angular momentum redistribution in the convective zone and changes in the magnetic field may cause differential rotation to become rigid. The latitudinal component angular momentum flow of meridional circulation is subject to Coriolis forces and turbulent Reynolds and Maxwell stresses. Maxwell stresses weakening the magnetic field are opposed by Reynolds stresses resulting in variance of the magnetic field and differential rotation. The differential rotation of Kepler-71 may be evidence of dominant Maxwell stresses.

There are, indeed, multiple ways to explain the almost rigid rotation observed. Given the potential impacts of core-coupling, star–planet interaction, Lorentz force effects, and Maxwell stresses, the essentially rigid rotation observed suggests that one or more of these physical mechanisms may be at work in the Kepler-71 system.

6 CONCLUSIONS

We have estimated the differential rotation of Kepler-71 by correlating the facula and starspot activity observed in sequential transits of Kepler-71b. Using the transit model described in Silva (2003), we detected and characterized 76 starspots and 52 faculae in 117 complete transits of Kepler-71 for 7 *Kepler* quarters. The photometric data noise limited the number of starspots and faculae which were discernable.

Our analysis presents the first use of faculae to measure stellar rotation period. The evidence of faculae, bright features seen on the transit light curves as a decrease in intensity as the planet transits over them, can be assured by (i) an increasing flux for faculae closer to the stellar limb, (ii) differing longitude distribution for spots and faculae, the latter being more prone to be detected closer to the limb, (iii) the area ratio of facula to spot is approximately 2, similar to the ratio found for solar-like active stars, and (iv) the rotation period estimated from faculae only is within 1 per cent of that obtained from spots. The properties listed as (i) and (ii) are those observed for solar faculae.

From autocorrelation of flux surplus for faculae as a function of longitude, we estimate the stellar rotation period to be 19.67 ± 0.05 d at the transit latitude. Autocorrelation of flux deficit for starspots yields the value 19.74 ± 0.05 d, within 1 per cent of the rotation period from faculae. Further, monitoring the signature of faculae and spots on four transits separated by five orbital periods each yields the rotation period of 19.71 d, whereas the out-of-transit mean rotation period is 19.77 d. Assuming a solar-like differential rotation profile (with increased rotation period away from the stellar equator), we calculate from faculae a weak rotational shear of $\Delta\Omega = 0.0052 \pm 0.0025$ rad d^{-1} and a relative differential rotation of $\Delta\Omega/\bar{\Omega} = 1.6 \pm 0.8$ per cent. The rotational shear and relative differential rotation calculated from spots yield similar values, $\Delta\Omega = 0.0015 \pm 0.0025$ rad d^{-1} and a relative differential rotation of $\Delta\Omega/\bar{\Omega} = 0.5 \pm 0.8$ per cent. Such low shear is in agreement with the presence of active longitudes that may be inferred from the spot transit mapping.

The rotational shear of Kepler-71 is relatively low as compared to the modest solar value of 0.055 rad d^{-1}. Multiple mechanisms which may result in the comparatively rigid rotation of Kepler-71 should be considered as contributors to this solar-type star's remarkably low differential rotation as compared to that of the Sun today.

ACKNOWLEDGEMENTS

The authors thank the anonymous referee for comments and suggestions that extended calculations and improved the content herein.

We also thank P. Wilson Cauley for providing an IDL implementation of the Goodman & Weare Monte Carlo Markov Chain.

AV acknowledges partial financial support from the Brazilian Research Funding Agency of the São Paulo State (FAPESP), # 2013/10559-5.

This paper includes data collected by the *Kepler* mission. Funding for the *Kepler* mission is provided by the NASA Science Mission directorate. *Kepler* light curve data was obtained from the NASA Exoplanet Archive, which provides public access to *Kepler* Mission data. The primary archive of all *Kepler* data is provided by the Mikulski Archive for Space Telescopes (MAST). STScI is operated by the Association of Universities for Research in Astronomy, Inc,. under NASA contract NAS5-26555. We thank the *Kepler* team for their efforts in providing the data and interfaces used in preparing this paper.

REFERENCES

Aigrain S. et al., 2015, MNRAS, 450, 3211
Ammler-von Eiff M., Reiners A., 2012, A&A, 512, A116
Balona L. A., Abedigamba O. P., 2016, MNRAS, 461, 497
Barnes J. R., Collier Cameron A., Donati J. -F., James D. J., Marsden S. C., Petit P., 2005, MNRAS, 357, L1
Berdyugina S. V., 2004, Sol. Phys., 224, 123
Berdyugina S. V., 2005, Living Rev. Sol. Phys., 2, 8
Bonomo A. S., Lanza A. F., 2012, A&A, 547, A37
Borucki W. J., 2010, Science, 327, 977
Bouvier J., 2013, Observational Studies of Stellar Rotation, EAS Publ. Ser. Vol. 62, Cambridge Univ. Press, Cambridge, p. 143
Carter B. D., , Marsden S. C., Waite I. A., 2015, in van Belle G. T., Harris H. C., eds, 18th Cambridge Workshop, Proceedings of conference held at Lowell Observatory, 8-14 June 2014, Cool Stars, Stellar Systems, and the Sun, p. 209

Christiansen J. L., Jenkins J. M., Caldwell D. A., 2012, PASP, 124, 1279
Covas E., 2017, A&A, 605, A44
Criscuoli S., Norton A., Whitney T., 2017, ApJ, 847, 93
Davenport J. R. A., Hebb L., Hawley S. L., 2015, ApJ, 806, 212
Estrela R., Valio A., 2016, ApJ, 831, 57
Foreman-Mackey D., Hogg D., Lang D., Goodman J., 2013, PASP, 125, 306
Giles H. A. C., Collier Cameron A., Haywood R. D., 2017, MNRAS, 472, 1618
Goodman J., Weare J., 2010, Commun. Appl. Math. Comput. Sci., 5, 68
Granzer. T., 2004, Astron. Nachr., 325, 417
Guenel M., Baruteau C., Mathis S., Rieutord M., 2016, A&A, 589, A22
Guinan E. F., Engle S. G., 2009, Proc. IAU Symp. 258, The Ages of Stars. Kluwer, Dordrecht, 395
Hackman T., Lehtinen J., Rosen L., Kochukhov O., Kapyla M., 2016, A&A, 593, A35
Hathaway D. H., 2015, Living Rev. Solar Phys., 12, 2
He H., Wang H., Yun D., 2015, ApJS, 221, 1
Hogg D. W., Foreman-Mackey D., 2018, ApJS, 236, 11
Holczer T. et al., 2015, ApJ, 807, 170
Howell S. B. et al., 2010, ApJ, 725, 1633
Hubbard A., Rheinhardt M., Brandenburg A., 2011, A&A, 536, A48
Isik E., Schmidtt D., Schussler L., 2011, A&A, 527, A135
Jenkins J. M. et al., 2010, ApJ, 173, L87
Kipping D. M., 2013, MNRAS, 435, 2152
Kobel P., Hirzberger J., Solanki S. K., 2018, preprint (arxiv:1410.5354)
Küker M., Rüdiger G., 2005, A&A, 422, 1023
Küker M., Rüdiger G., 2011, Astron. Nachr., 332, 933
Lanza A. F., 2010, A&A, 512, A77
Lanza A. F. et al., 2009, A&A, 506, 255
Lanza A. F. et al., 2009a, A&A, 493, 193
Lanza A. F. et al., 2011, A&A, 525, A14
MacGregor K. B., Brenner M., 1991, ApJ, 376, 204
Marsden S. C. et al., 2011, MNRAS, 413, 1939
Mathur S. et al., 2016, ApJS, 229, 30
Matt S. P., Do Cao O., Brown B. P., Brun A. S., 2011, Astron. Nachr., 332, 897
Maunder E. W., 1904, MNRAS, 64, 747
McQuillan A., Aigrain S., Roberts S., 2012, A&A, 538, A137
McQuillan A., Mazeh T., Aigrain S., 2013, ApJS, 775, L11
McQuillan A., Mazeh T., Aigrain S., 2014, ApJS, 211, 24
Mehrabi A., He H., Khosroshahi H., 2017, ApJ, 834, 207
Meibom S., Barnes S. A., Platais I., Gilliland R. L., Latham D. W., Mathieu R. D., 2015, Nature, 517, 589
Müller H. M. , Huber K. F. , Czesla S., Wolter U., Schmitt J. H M. M., 2013, A&A, 560, A112
Netto D. Y. S., Valio A., 2016, Young Stars & Planets Near the Sun, Proceedings of the International Astronomical Union, IAU Symp., vol. 314, p. 259
Ortiz A., Solanki S. K., Domingo V., Fligge M., Sanahuja B., 2002, A&A, 388, 1036
Press W. J., Teukolsky S. A., Vetterling W. T., Flannery B. P., 1992, Numerical Recipes in FORTRAN, The Art of Scientific Computing, 2nd edn. Cambridge Univ. Press, Cambridge
Reiners A., Schmitt J. H. M. M., 2002, A&A, 384, 155
Reinhold T., Reiners A., Basri G., 2013, A&A, 560, A4
Shapiro A. I., Solanki S. K., Krivova N. A., Yeo K. L., Schmutz W. K., 2016, A&A, 589, A46
Silva-Valio A., Lanza A. F., 2011, A&A, 529, A36
Silva-Valio A., Lanza A. F., Alonso R., Barge P., 2010, A&A, 510, A25
Silva A. V. R., 2003, ApJ, 585, L147
Smith J. C. et al., 2012, PASP, 124, 919
Spruit H. C., 1997, Mem. Soc. Astron. Ital., 68, 397
Spruit H. C., 2011, in Paz Miralles M., Sanchez Almeida J., eds, The Sun, the Solar Wind, and the Heliosphere, p. 39
Stumpe M. C. et al., 2012, PASP, 124, 984
Thomson, S. E., 2016, Kepler Data Release Notes (KSCI-19065-002)
Uzdensky D. Arons J., Balbus S., Blackman E., Goodman J., Medvedev M., Spitkovsky A., Stone J., 2010, Astro-2010 Decadal Science White Papers, Life Cycles of Magnetic Fields in Stellar Evoltuion
Valio A., 2013, ASP Conf. Ser. Vol. 472, New Quests in Stellar Astrophysics III: A Panchromatic View of Solar-Like Stars, With and Without Planets. Astron. Soc. Pac., San Francisco, 239
Valio A., Estrela R., Netto Y., Bravo J. P., de Medeiros J. R., 2017, ApJ, 835, 2
Varela J., Strugarek A., Brun A. S., 2016, Adv. Space Res., 58, 1507
Waite I. A., Marsden S. C., Carter B. D., Alecian E., Brown C., Burton D., Rhodes H., 2011, MNRAS, 413, 1939

This paper has been typeset from a TEX/LATEX file prepared by the author.